PCCP

Accepted Manuscript

ROYAL SOCIETY OF CHEMISTRY

www.rsc.org/pccp

PCCP

ARTICLE

Combined theoretical and time-resolved photoluminescence investigations of $[Mo_6Br^i_8Br^a_6]^{2-}$ metal cluster units: evidences of dual emission†

Received 00th January 20xx,
Accepted 00th January 20xx

DOI: 10.1039/x0xx00000x

www.rsc.org/

K. Costuas,*[a] A. Garreau,[b] A. Bulou,[c] B. Fontaine,[a] J. Cuny,[a, d] R. Gautier,[a] M. Mortier,[e] Y. Molard,[a] J.-L. Duvail,[b] E. Faulques*[b] and S. Cordier*[a]

The combined time-resolved photoluminescence (PL) and theoretical study performed on luminescent $[Mo_6Br^i_8Br^a_6]^{2-}$-based systems unambiguously show that their NIR-luminescence is due to at least two emissive states. By quantum chemical studies, we show for the first time that important geometrical relaxations occur at the triplet states by either the outstretching of an apex away from the square plane of the Mo_6 octahedron or by the elongation of one Mo-Mo bond. Experimental PL measurements demonstrate that the external environment (counter-ion, crystal packing) of the cluster has a noticeable impact on its relaxation processes. Temperature and excitation wavelength dependence of the two components of the luminescent spectra is representative of multiple competitive de-excitation processes in contradiction with the Kasha's rule. Our results also demonstrate that the relaxation process before and after emission can be tracked via fast time-resolved spectroscopies. They also show that the surrounding of the luminescent cluster unit and the excitation wavelength could be modulated for target applications.

Introduction

M_6L_{14} cluster units composed of metals of groups 6 and 7 (*i. e.* M = Mo, W, and Re; L = halogen and/or chalcogen) are versatile functional building blocks found in a tremendous range of inorganic solid-state compounds, in molecular and supramolecular assemblies, as well as in nanoparticles and nanocomposites.[1] In all these species, octahedral M_6 clusters are bonded to inner face-capping ligands (L^i) and apical ligands (L^a) to form face-capped $M_6L^i_8L^a_6$ cluster units (L = halogen and/or chalcogen) (Fig. 1A). In the solid-state, condensation of these units can occur via direct metal-metal bonds or via chalcogen bridges. This enables electronic interactions between units with the formation of a band-based electronic structure. The resulting materials can thus exhibit transport properties and even superconducting transitions at low temperature depending on the electron population of the conducting and valence bands. Thermoelectricity,[2] cation sensoring and electronic and ionic conductivity were reported as technological application for those systems.[3]

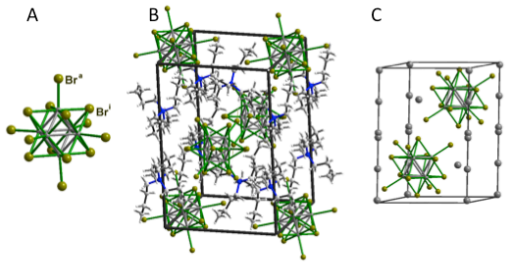

Fig. 1 (A) Geometry arrangement of the $[Mo_6Br^i_8Br^a_6]^{2-}$ cluster unit. Representation of the crystal structure of (B) $(TBA)_2[Mo_6Br^i_8Br^a_6]$ and (C) $(Cs)_2[Mo_6Br^i_8Br^a_6]$.[12] Note that for the latter, one crystallographic position is statistically occupied at 50% by Cs.

Additionally, many soluble $A_x[M_6Q^i_8L^a_6]$ molecular solids built up from discrete $[M_6Q^i_8L^a_6]^{n-}$ units are reported in the literature (see Fig. 1A for illustration). Among them, the isoelectronic $[M_6X^i_8L^a_6]^{2-}$ (M = Mo or W) and $[Re_6Q^i_8L^a_6]^{4-}$ cluster units (X = Cl, Br and I; Q = S, Se or Te; L = halogen, OH, CN, N_3, NCS or functional organic moiety) units[4] exhibit interesting physico-structural properties. Their optical properties are particularly interesting. Most of them present a large absorption window from Ultra Violet (UV) to the visible (vis.) and a large characteristic emission window from vis. to near Infra Red (NIR). This makes for example M_6 clusters particularly well-suited luminescent dyes for the elaboration of multifunctional nanoparticles for bio-labeling.[5] The added value compared to their organic homologs, is that they show negligible

[a] Institut des Sciences Chimiques de Rennes, CNRS - ENSC Rennes - Université de Rennes, France. Email: kcostuas@univ-rennes1.fr; stephane.cordier@univ-rennes1.fr
[b] Institut des Matériaux Jean Rouxel, Université de Nantes, CNRS, France. Email: eric.faulques@cnrs-imn.fr
[c] Institut des Molécules et Matériaux du Mans/PEC, Université du Maine, CNRS, France
[d] Laboratoire de Chimie et Physique Quantiques, IRSAMC, Université Paul Sabatier, 118 Route de Narbonne, 31062 Toulouse Cedex 4, France
[e] Institut de Recherche de Chimie Paris, Chimie ParisTech, CNRS, France

† Electronic Supplementary Information (ESI) available: experimental and calculated absorption and emission spectra of $[Mo_6Br^i_8Br^a_6]$-containing systems, TD-DFT electronic excitations calculated for $[Mo_6Br^i_8Br^a_6]^{2-}$ (O_h DFT optimized geometry) and its experimental $(TBA)_2[Mo_6Br^i_8Br^a_6]$ arrangement, simulated absorption spectra of T_1, T_2, T_3, T_4. See DOI: 10.1039/b000000x

photobleaching and have a lower toxicity.[5b-c] Combination of Mo_6-based building blocks with mesogenic organic partners leads to a new class of liquid crystal, namely the clustomesogens, that exhibits potential applications in LCD and lighting displays.[6] Recent development in the field of cluster-based hybrid copolymers evidenced potential applications in energy conversion. Indeed, they can be used as solar cell concentrators to improve the efficiency of Si-based photovoltaic cells.[7] Recently, they were used as sensitizers of the NIR luminescence of erbium cations for the design of Band-C telecom amplifiers.[8] Tunable visible emission can be obtained by combining Mo_6 clusters with other luminophors, nanoparticules or other nanosources, that exhibit complementary emission window. For instance, colloids and nanoparticles made of Mo_6 clusters absorbed on ZnO nanocrystals were recently prepared and showed a stable white light emission.[9] Similarly, polymer nanocomposites can be prepared leading for example to tunable yellow/green emissive co-axial nanowires made of poly(paraphenylene-vinylene) and Mo_6 cluster-containing PMMA.[8,10] Concerning their chemical properties, Mo_6 clusters immobilized on graphene oxide show interesting photo-catalytic properties (degradation of pollutants and photo-reduction of CO_2).[11]

In 1981, H. B. Gray *et al.* reported for the first time that $[Mo_6X^i_8X^a_6]^{2-}$ clusters were among the brightest transition metal-based luminophors with quantum yield reaching 0.23 for $[Mo_6Br^i_8Br^a_6]^{2-}$ clusters.[13] They showed that the luminescence of $[Mo_6Cl^i_8Cl^a_6]^{2-}$ and $[Mo_6Br^i_8Br^a_6]^{2-}$ is red-shifted at low temperatures with a narrowing of the emission band.[4a] Similar emission properties for $[Mo_6I^i_8I^a_6]^{2-}$ iodide homolog were latter reported.[4f,14] The measurement of quantum yield and lifetimes of those systems were revisited recently in the same experimental condition and in solution. It turns out that quantum yields decrease from 0.15 to 0.12 going from X = Cl to I whilst the lifetimes decrease from 180 to 90 µs.[4f] The luminescence of M_6 clusters is closely related to the metal nature. Indeed, changing the metal atom from molybdenum to tungsten results in species for which the nature of the ligands has a stronger and an opposite influence on the quantum yields and lifetimes. When going from Cl to I in the $[W_6X^i_8X^a_6]^{2-}$ series, quantum yield increases from 0.02 to 0.39 and lifetime increases from 1.5 to 30 µs. This illustrates the fact that the photophysical properties of octahedral metal clusters needs to be studied individually.

Several groups tried to rationalize these optical features but no fully comprehensive explanation has been given to date. T. Azumi *et al.* proposed a phenomenological approach in which they consider that emission originates from the thermal population of spin-orbit-split excited states.[15] Later, D. E. Ellis *et al.* published X_α calculations of $[Mo_6Cl^i_8Cl^a_6]^{2-}$ from which they estimate the emission wavenumber, but it deviates of 0.9 eV from experimental data.[16] More recently, R. Arratia-Pérez and co-workers calculated excitation energies of the complete $[Mo_6X^i_8X'^a_6]^{2-}$ series via spin-orbit time-dependent density functional calculations but they did not calculate the emission ones.[17]

Thus, despite the diversity of materials that incorporate molybdenum octahedral clusters as functional building blocks, their photophysical properties are not fully understood. This constitutes an impediment to fully exploit their capabilities and thus for the development of cluster-based nano-composites. As established by T. G. Gray, combined theoretical and time/temperature-dependent spectroscopic investigations are compulsory to elucidate the mechanisms responsible for the unique luminescence of octahedral transition metal clusters.[18] Isoelectronicity cannot be simply applied to rationalize their photophysical properties.

In this work, we use an efficient methodology combining quantum chemistry studies and spectroscopic investigations to evaluate the influence of temperature and excitation wavelength on the emission properties (lifetime, intensity, emission wavelengths) of two $[Mo_6Br^i_8Br^a_6]^{2-}$ based systems. On one hand, the cluster unit is associated with an organic counter-ion $(n\text{-}C_4H_9)_4N^+$ $(TBA)^+$, $(TBA)_2[Mo_6Br^i_8Br^a_6]$, and, on the other hand, with an inorganic one, Cs^+, $(Cs)_2[Mo_6Br^i_8Br^a_6]$ (see Fig. 1). Those systems are studied both in solution and in the solid-state. For the first time, luminescence properties are investigated in a continuous range of excitation wavelength (from 250 to 550 nm). Quantum chemical studies reveal that several triplet excited states are involved. Indeed, important geometrical relaxations are found explaining the origin of the unusual emission properties of the studied compounds.

Experimental

A General considerations

$(Cs)_2[Mo_6Br^i_8Br^a_6]$ and $(TBA)_2[Mo_6Br^i_8Br^a_6]$ are particularly well suited for spectroscopic investigations because of their high chemical stability. They were prepared and purified according to the procedures reported in the literature.[12a] The X-Ray powder diffraction patterns did not reveal the presence of any impurity. The high purity powder samples of $(Cs)_2[Mo_6Br^i_8Br^a_6]$ and $(TBA)_2[Mo_6Br^i_8Br^a_6]$ was confirmed by Raman spectroscopy analysis. Those results are consistent with the data reported by Bublitz and Preetz.[19] In the case of $(Cs)_2[Mo_6Br^i_8Br^a_6]$, the whole set of Raman lines predicted from the structure is observed and attributed from polarized studies on single crystals.[20]

B Structural description and considerations

Both $(Cs)_2[Mo_6Br^i_8Br^a_6]$ and $(TBA)_2[Mo_6Br^i_8Br^a_6]$ are built up from $[Mo_6Br^i_8Br^a_6]^{2-}$ cluster units. $(Cs)_2[Mo_6Br^i_8Br^a_6]$ crystallizes in the *P*-31*c* space group (n° 163) with the following lattice parameters: a = 10.1925(1) Å, c = 15.0690(3) Å, V = 1355.74 Å^3, Z = 2 (see Fig. 1C).[12] The cluster units are arranged according to a *A-B-A-B* close-packed hexagonal stacking. Indeed strong electrostatic interactions occur between Cs^+ cations and bromine ligands. On the other hand, $(TBA)_2[Mo_6Br^i_8Br^a_6]$ crystallizes in the $P2_1/n$ space group (n°

14) with the following lattice parameters: a = 13.2110(2) Å, b = 11.8530(2) Å, c = 18.9280(4) Å, β = 90.843(1)°, V = 2963.61(9) Å^3, Z = 2 (see Fig. 1B). Stacking of $[Mo_6Br^i_8Br^a_6]^{2-}$ cluster units corresponds to a distorted centered cubic arrangement. Owing to the bulkiness of $(TBA)^+$ compare to Cs^+, it turns out that the cluster-density in $(TBA)_2[Mo_6Br^i_8Br^a_6]$ is less than that of $(Cs)_2[Mo_6Br^i_8Br^a_6]$ as reflected by the unit cell volumes. Moreover at room temperature (RT), X-Ray structural investigation evidenced a strong disorder of alkyl chain of the TBA ions.

C Solid-state photoluminescence excitation maps

We carried out solid-state PL excitation maps using a Jobin-Yvon Fluorolog 3 equipped with a CCD camera at RT in a range of excitation 250-550 nm onto cluster powders previously deposited onto quartz substrate by spin coating (5 mg/ml acetone, 2000 rpm/min, 30 s). The mapping allows to visualize both PL excitation and emission ranges, and to determine the variation of the emission spectrum against the excitation energy.

D Variable-Temperature solid-state photophysical measurements

The transient PL experiments have been achieved under 400 nm excitation using a Spectra-Physics Hurricane X laser system (82 fs, 1 kHz) onto cluster powder previously deposited onto suprasil® quartz substrate. The collected emission was temporally detected with a streak camera (Hamamatsu C7700, see Fig. S4 for apparatus corrections) coupled with an imaging spectrograph. The laser pump power impinging on sample was kept at 4 mW. Temperature measurements were conducted by attaching the sample on a cold finger with a heat transfer metal (indium) near a nominal-temperature AsGa diode in a vacuum loading, helium-cooled, continuous flow shielded cryostat down to 12 ± 0.5 K.

E Solution absorption and emission measurements

UV-vis. absorption spectra were recorded with a Varian CARY 5 spectrometer. The emission spectra were recorded using a Cary Varian spectrophotometer (Eclipse). Two solvents were used: acetone and acetonitrile (dielectric constant ε = 20.7 and 37.5 F.m^{-1} respectively; dipole moment μ = 2.86 and 3.45 D, resp.).

F Computational details

DFT calculations on the $[Mo_6Br^i_8Br^a_6]^{2-}$ molecular unit were carried out using the Amsterdam Density Functional (ADF 2014.01) program package developed by Baerends and co-workers.[21] The revPBE exchange and correlation non-local gradient corrections[22] were included in the local density approximation.[23] Relativistic spin-orbit (SO) coupling was treated by a first-order perturbation theory from a ZORA Hamiltonian.[24] The all electron ADF QZ4P basis set was used, i.e., a quadruple-ζ STO basis set completed with four polarization functions. Tamm-Dancoff approximation SO calculations were used to evaluate the lifetime of the excited states and the oscillator strength.[25] In that case, two-component spin−orbit coupling calculations were performed.[26]

Geometry optimization of the crystal structure $(TBA)_2[Mo_6Br_{14}]$ was carried out using the CASTEP 6.0 code[27] by using the PBE functional.[28] Dispersion corrections were added in the calculations following the procedure proposed by Tkatchenko and Scheffler.[29] The convergence was reached with a minimum cut-off energy of 500 eV. Four irreducible k points were used. All ultra-soft pseudopotentials were generated by using the OTF ultrasoft pseudo-potential generator included in CASTEP 6.0. Relativistic effects were included for all elements during the US-PP generation by solving the radial scalar relativistic equation of Koelling and Harmon.[30] Since cell parameters are in principle the crystallographic data that are determined with the best accuracy and because geometry optimization of both cell parameters and atomic positions would necessitate a huge computational effort, only atomic positions were optimized.

Results

A Absorption and emission properties in solution at room temperature

$[Mo_6Br^i_8Br^a_6]^{2-}$ in solution absorbs strongly in the UV-region.[4a] It has to be emphasized that absorbance is also present in the visible-region. The inset of Fig. S1 shows that the lower limit of absorption can be considered around 20000 cm^{-1}. Indeed, the absorption spectrum of $[Mo_6Br^i_8Br^a_6]^{2-}$ reveals that the cluster unit absorbs intensively and continuously in a large optical region lying between the UV to the vis. region. These absorption properties are hardly influenced by the nature of the counterion, nor by the nature of the solvent (polarity, coordinating ability) (see experimental section and supporting information). This also reveals that no ion-pairing occurs and that the absorption in the vis. region is only due to the $[Mo_6Br^i_8Br^a_6]^{2-}$ units.

The luminescence spectra of acetone and acetonitrile solution of $(Cs)_2[Mo_6Br^i_8Br^a_6]$ and $(TBA)_2[Mo_6Br^i_8Br^a_6]$ and their characteristics are given in Fig. 2, Fig S2 and Table S1. As for absorption, the emission spectra are almost identical whatever the nature of counterion or of the solvent, probing the absence of ion-pairing in the excited state. Emission is intense from the red to the NIR region with a maximum located at 740 nm (13540 cm^{-1}). As shown in Fig. 2, this emission signal necessitates two Gaussian curves to be correctly fitted, one centered at 729 and the other at 809 nm (full width at half maximum (FWHM) 3310 and 1140 cm^{-1} resp.).

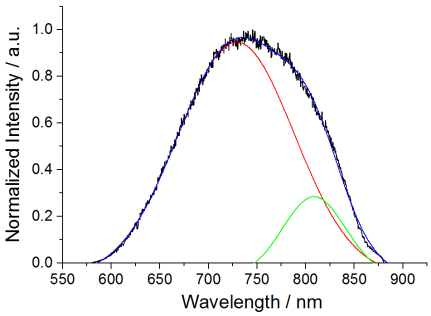

Fig. 2 RT emission spectra of acetone solution of $(Cs_2)[Mo_6Br^i_8Br^a_6]$ in (black) (concentration: 2.10^{-6} mol.L^{-1}, excitation wavelength 355 nm). This spectrum was fitted with Gaussian functions (red and green lines). The cumulative fit is plotted in blue.

B Absorption and emission properties in solid-state

The solid-state optical properties of $(TBA)_2[Mo_6Br^i_8Br^a_6]$ and $(Cs)_2[Mo_6Br^i_8Br^a_6]$ were investigated by two technics. First, steady-state PL experiments according to the excitation wavelengths we recorded at RT. Additionally, in order to gain some insights on the de-excitation processes, time-resolved PL spectroscopic experiments were performed at RT and 12 K.

Steady-state photo-luminescence cartography. PL cartography of $(TBA)_2[Mo_6Br^i_8Br^a_6]$ and $(Cs)_2[Mo_6Br^i_8Br^a_6]$, recorded at RT are shown in Fig. 3. The PL of the two compounds do not depend significantly on the excitation energy (see normalized excitation spectra in Fig. S3). Fig. 3 shows that the PL spectra are similar, both in intensity and emission wavelength for excitations ranging from 480 to 380 nm (20830 to 26320 cm^{-1}). The PL profiles can be fitted by two Voigt components (see Table 1). These components appear at room temperature around 722 nm (13850 cm^{-1}) and 856 nm (11680 cm^{-1}) for $(TBA)_2[Mo_6Br^i_8Br^a_6]$ whatever the excitation energy, whereas in $(Cs)_2[Mo_6Br^i_8Br^a_6]$ the second component slightly changes from 844 to 855 nm (11700 to 11850 cm^{-1}) when decreasing of the excitation energy. The full-width at half-maximum (FWHM) of the second component is larger than its counterpart in $(TBA)_2[Mo_6Br^i_8Br^a_6]$ (see Table 1), revealing a noticeable influence of the crystal environment on the cluster units luminescent properties that are depicted above.

Cartographies show a PL intensity depletion between 455 and 465 nm (see Fig. S3). In the case of $(Cs)_2[Mo_6Br^i_8Br^a_6]$, a small blue shift of 110 cm^{-1} of the second component accompanies this lowering of intensity. The intensity gradually rises again when the excitation energy decreases. A second decrease in intensity is observed around 480-490 nm. The PL vanishes gradually for excitation wavelengths higher than 505 nm for TBA-containing powder and 510 nm for Cs-containing one.

Whereas no significant energy variation of the two PL components for $(TBA)_2[Mo_6Br^i_8Br^a_6]$ is observed during this last process, the second PL component **2** for $(Cs)_2[Mo_6Br^i_8Br^a_6]$ is gradually blue-shifted (at 856 nm for 450 nm excitation to 828 nm for 510 nm excitation, c. a. 395 cm^{-1} of shift). The evolution of the contribution of each component is far to be linear and depends on the excitation wavelength. This unambiguously reveals competitive non-radiative de-excitation processes.

Table 1 Peak positions, FWHM in nm and relative contribution (cont. 1 and cont. 2) for $(TBA)_2[Mo_6Br^i_8Br^a_6]$ (top) and $(Cs)_2[Mo_6Br^i_8Br^a_6]$ (bottom) of the two Voigt components **1** and **2** of the fitted emission spectra in Fig. 3 at different excitation wavelengths (nm). In each case, the coefficient of determination R^2 is reported.

$(TBA)_2[Mo_6Br^i_8Br^a_6]$

λ_{Exci}	380	400	420	450	460	480	505
Max. 1	722.0	721.9	722.2	722.3	721.0	722.1	722.2
Max. 2	855.8	855.7	857.8	858.7	858.8	855.8	858.1
FWHM 1	165.6	132.2	166.6	156.4	141.3	152.0	142.0
FWHM 2	165.8	164.6	149.0	158.1	165.0	167.7	171.2
Cont. 1	0.62	0.61	0.62	0.62	0.59	0.61	0.57
Cont. 2	0.38	0.39	0.38	0.38	0.41	0.39	0.43
R^2	0.999	0.999	0.999	0.999	0.999	0.999	0.999

$(Cs)_2[Mo_6Br^i_8Br^a_6]$

λ_{Exci}	380	400	420	450	460	480	510
Max. 1	718.8	719.8	721.8	721.7	720.0	721.9	717.0
Max. 2	844.5	848.4	855.2	856.0	848.1	855.4	828.0
FWHM 1	155.1	135.4	162.6	132.3	135.4	133.7	127.6
FWHM 2	200.4	189.4	166.9	170.6	201.2	172.9	237.7
Cont. 1	0.51	0.54	0.58	0.57	0.82	0.51	0.41
Cont. 2	0.49	0.46	0.42	0.43	0.18	0.49	0.59
R^2	0.999	0.999	0.999	0.999	0.999	0.999	0.998

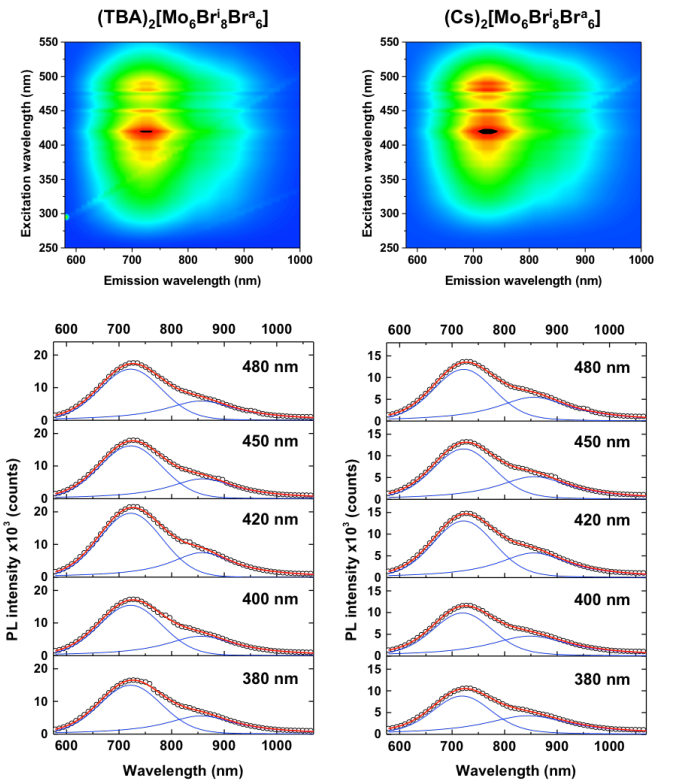

Fig. 3 Solid-state PL excitation maps measured at 293 K for $(TBA)_2[Mo_6Br^i_8Br^a_6]$ (left) and $(Cs)_2[Mo_6Br^i_8Br^a_6]$ (right) and emission spectra (black circles) at 380, 400, 420, 450, and 480 nm excitation wavelengths. These spectra were fitted with Voigt functions (blue solid lines). The cumulative fits are plotted in red.

Temperature dependence of the time-resolved PL (TRPL). TRPL of $(TBA)_2[Mo_6Br^i_8Br^a_6]$ and $(Cs)_2[Mo_6Br^i_8Br^a_6]$ were investigated in the solid-state with an excitation of 400 nm

(25000 cm^{-1}) at RT and 12 K. Normalized emission spectra and associated PL decay curves are shown in Fig. 4 for both systems at the two extreme temperatures. A noticeable red-shift of the emission band is observed in both cases upon temperature-lowering associated with a decrease of the FWHM. As expected, the decay time increases upon temperature lowering. Moreover, it is cation-dependent as detailed below.

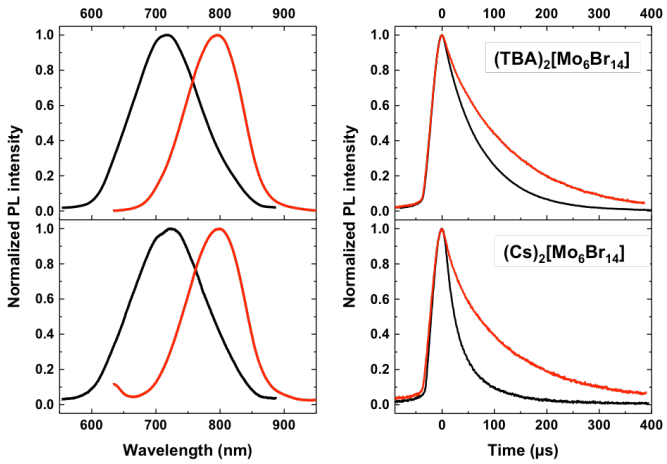

Fig. 4 Normalized emission spectra (left) and associated PL decay curves (right, integrated in all spectral range) of $(TBA)_2[Mo_6Br^i_8Br^a_6]$ (top) and $(Cs)_2[Mo_6Br^i_8Br^a_6]$ (bottom) recorded at RT (black) and 12 K (red) under a pulsed 400 nm excitation.

The contributions to emission of the two spectral components for each system versus time and temperature are reported in Fig. 5 and 6. The decay curves shown in these figures have been integrated in a narrow region of interest of 4 nm width at the maximum emission of each component and compared to the full decay profiles. The results are summarized in Table 2. There is no difference between the temporal evolution of the full spectrum and that of each spectral component at the same temperature (RT or 12 K). $(Cs)_2[Mo_6Br^i_8Br^a_6]$ exhibits the highest PL lifetime increase from room temperature to 12 K.

Overall, the TRPL measurements reveal several striking features. First, the spectral distribution of the phosphorescence signal, for both compounds, is at least composed of two distinct components, as confirmed by the spectral profile fits (see Fig. 5, 6 and Table 2). Therefore, PL emission from a single excited state should be ruled out. The PL profile presumably stems from the emission of several excited states close in energy. Their relative population depends on temperature and their wavelength is red-shifted as they are depopulated.

Secondly, the PL emission energy and the PL bandwidths of the two cluster solid-state compounds are similar. Moreover, steady-state PL experiments suggest that the emission is hardly dependent on the excitation energy for values ranging between 380 and 480 nm (26320 and 20830 cm^{-1}) (see Table 1). Therefore, the characteristics of the solid-state PL of these materials and their inherent physical mechanisms appear to prominently originate from the $[Mo_6Br^i_8Br^a_6]^{2-}$ anion.

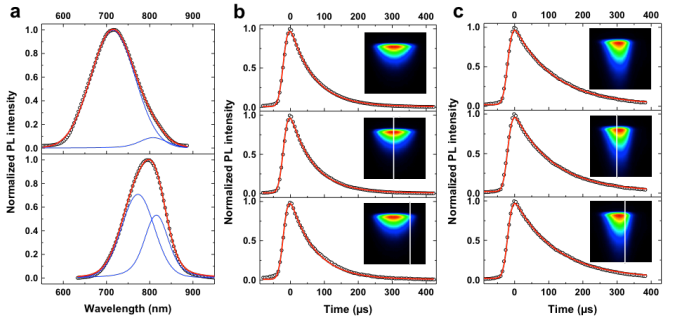

Fig. 5 (a) $(TBA)_2[Mo_6Br^i_8Br^a_6]$ emission spectra (black circle) measured at RT (top) and 12 K (bottom) fitted with two Voigt components (blue solid lines) and the cumulative fits obtained (red) under 400 nm excitation. Associated PL decay curves at RT (b) and at 12 K (c), integrated: in the whole spectral range (top), at the wavelength of the maximum of first Voigt function (middle), at the wavelength of the maximum of the second Voigt function (bottom) as illustrated in inset (4 nm spectral widths). In each case, circles and solid lines correspond to experimental points and fitted curves, respectively.

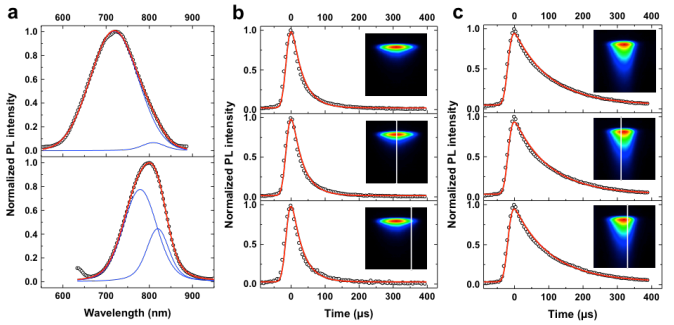

Fig. 6 $(Cs)_2[Mo_6Br^i_8Br^a_6]$ emission spectra and associated PL decay curves. (a), (b), (c) see Fig. 5.

The maximum energy of the observed PL bands is red-shifted as the temperature is lowered from RT to 12 K. In TRPL, this shift is of 1360 and 1350 cm^{-1} for both $(TBA)_2[Mo_6Br^i_8Br^a_6]$ and $(Cs)_2[Mo_6Br^i_8Br^a_6]$ respectively (spectral resolution of 50 cm^{-1} in that region). It has to be noted that, at RT, the second component of the PL is more red-shifted in the steady-state PL spectra than in the TRPL experiment (see Tables 1 and 2). This discrepancy in the spectral profile is mainly due to the irradiation procedure that is pulsed (femto-second laser) in the TRPL and continuous for a PL cartography recording (about 10 min with wavelength changes). For the latter, excited states that are formed can also absorb and relax modifying the global emission response. It has to be stressed that in this part of the spectrum no wavelength correction (possible apparatus response) are needed (see Fig. S4).

The dependence against temperature of the maximum wavelengths λ_1 and λ_2 of the two extracted components **1** and **2** for both clusters shows a concomitant and monotonically increase without anomalous behavior, except for the last point (See Fig. 7). The red-shift of the phosphorescence band observed upon temperature lowering is clearly an indication that vibronic contributions are not at the origin of this emission changes (it would be the reverse in that case). The second component λ_2 is less affected upon temperature lowering than λ_1 which is in contradiction with a gradual sensitivity loss in the

near IR range. λ_2 might be underestimated but changes in de-excitation processes upon temperature can also be argued.

Table 2. Peak positions, FWHM in nm, contribution (cont.) and decay times in µs of the components **1** and **2** obtained from the fit of TRPL spectral and temporal curves of $(TBA)_2[Mo_6Br^i_8Br^a_6]$ and $(Cs)_2[Mo_6Br^i_8Br^a_6]$ presented in Fig. 5 and 6. In each case, the coefficient of determination R^2 is reported.

	$(TBA)_2[Mo_6Br^i_8Br^a_6]$		$(Cs)_2[Mo_6Br^i_8Br^a_6]$	
T (K)	RT	12 K	RT	12 K
λ_{Max}	718	796	722	800
λ_1	715	773	719	779
λ_2	808	815	809	820
FWHM 1	120	89	130	102
FWHM 2	76	66	64	61
Cont. 1	0.94	0.61	0.96	0.70
Cont. 2	0.06	0.39	0.04	0.30
R^2	0.999	0.999	0.999	0.999
τ	69.5	116.2	33.5	104.2
R^2	0.999	0.999	0.995	0.997
τ_1	67.9	113.5	33.3	102.1
R^2	0.999	0.999	0.996	0.996
τ_2	72.1	121.4	33.0	105.2
R^2	0.997	0.998	0.994	0.994

Upon lowering of temperature between RT and 12 K, it is worth noticing that the increase of lifetime in $(TBA)_2[Mo_6Br^i_8Br^a_6]$ is about 45-50 µs, while in $(Cs)_2[Mo_6Br^i_8Br^a_6]$ it is around 72 µs. Note that the lifetime measurement uncertainty is ±2 µs. This increase of lifetime is thus reliable. The fact that the evolution of lifetime is remarkably similar for τ (full PL band) and also for τ_1 and τ_2 (1st and 2nd PL components) for both systems is an indication for a possible common physical process. While the cationic environment seems to have no apparent effect on the emission energy and the spectral red-shift in the TRPL experiment, it has obviously an influence on the PL quenching. Whatever the temperature, the absolute values of lifetimes in $(Cs)_2[Mo_6Br^i_8Br^a_6]$ are shorter than in $(TBA)_2[Mo_6Br^i_8Br^a_6]$, even if they are in the same range. This means that more non-radiative paths, due to vibrations, are involved in the $(Cs)_2[Mo_6Br^i_8Br^a_6]$ de-excitation process than in the $(TBA)_2[Mo_6Br^i_8Br^a_6]$ one.

C Density functional study

Quantum chemical calculations were performed in order to give a more precise description of the absorption and phosphorescence phenomenon of the $[Mo_6Br^i_8Br^a_6]^{2-}$ containing systems.

Structural studies. Several experimental facts allowed us considering that the absorption properties of $[Mo_6Br^i_8Br^a_6]^{2-}$ containing systems are essentially due to the cluster unit itself. Indeed, the absorption spectra in solution are identical whatever the nature of the counterion (i. e. TBA^+ or Cs^+) and the concentration does not modify the absorption wavelengths. This indicates that neither ion-pairing nor aggregation are occurring. The X-Ray characterizations of $(TBA)_2[Mo_6Br^i_8Br^a_6]$ and $(Cs)_2[Mo_6Br^i_8Br^a_6]$ reveal that the cluster units do not exhibit an ideal O_h symmetry but adopt C_i and D_{3d} symmetry respectively. Raman scattering studies of oriented $(Cs)_2[Mo_6Br^i_8Br^a_6]$ single-crystals under polarized light at low temperature clearly show breaking of the O_h symmetry of $[Mo_6Br^i_8Br^a_6]^2$ in the solid-state (with for example narrow well resolved multiplets arising from triply degenerate modes in the cubic symmetry; see general considerations). Packing effects and more particularly electrostatic interactions with the Cs^+ ions are at the origin of this deviation. The experimental optical measurements in the solid-state show small changes depending on the counterion nature (see Table 2). A complete understanding of the intrinsic optical properties of the $[Mo_6Br^i_8Br^a_6]^{2-}$ unit is required in order to distinguish the role of each external factor.

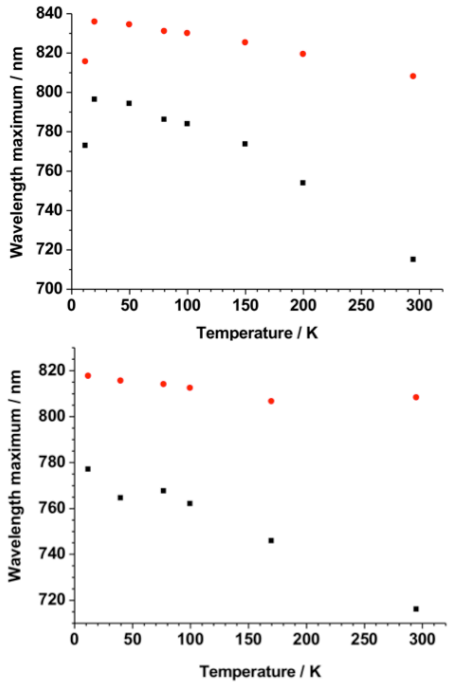

Fig. 7 Wavelength components of phosphorescence vs. observation temperature in $(TBA)_2[Mo_6Br^i_8Br^a_6]$ (top) and $(Cs)_2[Mo_6Br^i_8Br^a_6]$ (bottom) extracted from Voigt fits to the transient spectral PL data.

In order to elucidate the structural arrangement of the discrete unit, geometry optimizations of $[Mo_6Br^i_8Br^a_6]^{2-}$ unit were performed (see Computational details). For the ground state, O_h symmetry geometry was found to be the global minima according to the vibrational frequency analysis. The optimized geometry of the $[Mo_6Br^i_8Br^a_6]^{2-}$ isolated unit has Mo-Mo, Mo-Br^i, and Mo-Br^a averaged distances that deviate from 0.02 to 0.05 Å from the experimental X-Ray solid-state data (less than 2%) (see Table S2). Arratia-Pérez and coworkers published in 2008 a DFT study devoted to the electronic excitations of $[Mo_6X^i_8X^a_6]^{2-}$ units (X = halogen) in which an optimized ground state geometry of $Mo_6Br_{14}^{2-}$ unit was reported.[17] In that study, the Mo-Mo distances are 0.02 Å longer than the X-Ray structures. It has to be noted that the local density approximation (LDA) was used for the DFT calculations. This latter is known to always give shorter metal-metal distances because of error compensations. Indeed, metal-halogen distances are less well reproduced than in our calculations, with the inner bond lengths calculated 0.08 Å shorter than the

experimental ones. The level of theory used here describes better the metal-halogen interactions, which is of importance for the excited state calculations.

In order to assess the effects of the crystal packing on the geometry of the Mo_6 units, the crystal structure of $(TBA)_2[Mo_6Br^i_8Br^a_6]$ has been optimized. In a crystalline structure, the cell parameters are the crystallographic data that are determined with the best accuracy. Thus we only optimized the atomic positions using the crystallographic cell parameters. Structural parameters resulting from these geometry optimizations are given in Table S2. The crystalline and molecular Mo-Mo optimized bond lengths are comparable and agree very well with the experimental values. Mo-Br distances compare even better with experimental values than with the ones resulting from molecular calculations. The $[Mo_6Br^i_8Br^a_6]^{2-}$ unit structural arrangement of the optimized $(TBA)_2[Mo_6Br^i_8Br^a_6]$ slightly deviates from O_h as found experimentally. The calculated distances are indeed in very good agreement with the X-Ray structure validating our theoretical methodology both for the discrete cluster unit and its solid-state structures.

Molecular electronic structure of $[Mo_6Br^i_8Br^a_6]^{2-}$. Face-capped octahedral transition metal cluster units have been the subjects of various theoretical investigations.[31] From a qualitative point of view, the electronic structure of groups 6 and 7 transition metals M_6 clusters are very similar regardless of the nature of the capping and apical ligands: twelve molecular orbitals (MOs) mainly centered on metals have mainly a metal-metal bonding character and to a lesser extent a metal-ligand antibonding one. They are well separated from antibonding MOs by a significant energy gap.[32] The optimal electron count of such arrangements that is the one corresponding to the occupation of these bonding MO (the metal-metal antibonding MO being vacant) is equal to 24 in the case of $[Mo_6X^i_8X^a_6]^{n-}$. It is achieved for a charge n equal to 2. Energies and occupancies of the frontier MOs of $[Mo_6Br^i_8Br^a_6]^{2-}$ species optimized under O_h symmetry are in full agreement with the previously published studies, the highest occupied MOs being mainly localized on the metal atoms and to a lesser extent on the halogen ligands. They are metal-metal (d/d) bonding and metal-ligand anti-bonding (d/π*). The first unoccupied MOs are the antibonding metal-metal MO counterparts, still presenting metal ligand anti-bonding (d/π*) character.[31]

The octahedral symmetry of the isolated $[Mo_6Br^i_8Br^a_6]^{2-}$ unit is undoubtedly the ground state (S_0) structural arrangement (in vacuum at 0 K). Nevertheless, experimentally, the anisotropy of the cluster environment induces slight deviations from O_h symmetry. In solution, the interaction with the solvent and the vibrational motions due to temperature lead to slight deformations of the cluster geometry. In the solid-state, the packing effects, especially the counter-ion arrangements and their electrostatic interactions with the cluster unit create symmetry breakings. The spatial extensions of those MOs are thus slightly modified by the deviation to O_h symmetry, allowing small admixtures between electronic levels.

Electronic excitations. These tiny deviations from O_h symmetry are indeed compulsory to understand the optical properties of $[Mo_6Br^i_8Br^a_6]^{2-}$ containing systems. Indeed, TD-DFT calculations were performed starting from the optimized O_h symmetry and from the solid-state structures. The complete results are reported in Supporting Information. These calculations provide the vertical energies of the first excited states that are the Franck-Condon (FC) excited states. Most of the lowest energy singlet-singlet excitations that range between 20080 to 32170 cm^{-1} (497 to 311 nm) are symmetry-forbidden in O_h symmetry (the oscillator strengths associated to these absorptions are strictly zero), except for T_{1u} symmetry excitations which have oscillator strengths lower than 0.01 (see Table S3). Nevertheless, the experimental UV-vis. absorption spectra measured in solution show a continuous but small absorbance in that energy region (see Fig. S1). This is due to deviations from O_h symmetry explained here above. We thus performed TD-DFT calculation using the structural arrangement determined by X-Ray investigations that presents the lower symmetry (i. e. $(TBA)_2[Mo_6Br^i_8Br^a_6]$ of C_i symmetry) to introduce symmetry breaking. Solvent effects were included for comparison purpose with the experimental spectrum (see Computational Details). In that case, the oscillator strengths of 19 electronic excitations over 213 are above 0.01. Moreover, the rest of the excitations are not strictly forbidden. The superposition of those excitations explains the small experimental absorptions measured at low energy (See Fig. S5). These corresponds to metal to metal transitions, from bonding to antibonding character. Indeed, these excited states can be described formally as the result of the population of the first anti-bonding MOs of the LUMO region.

Concerning the singlet-triplet excitations, they are spin-forbidden if SO coupling is not significant. The probability to be populated by photon absorption is almost inexistent. Nevertheless, triplet states can be populated indirectly via an intersystem crossing process that follows non-radiative de-excitations (internal conversion) between singlet-singlet states. Following the Kasha's Rule (which is a postulate), the lowest triplet state should be populated. The lower lying triplet state FC-T_1 is calculated more stable than the lowest singlet state FC-S_1 (19276 vs 20099 cm^{-1}, see Table S3 and S4) mainly because of the extra stabilization given by the exchange part of the energy. This energy is far above the experimental emission energies that are ranging from 11000 to 14700 cm^{-1}.

PCCP

ARTICLE

Table 3. Mo-Mo, Mo-Br^{i}, and Mo-Br^{a} distances (in Å) of DFT-optimized ground state (S_0) and of the first excited triplet (T_1, T_2, T_3, T_4) of $[Mo_6Br^{i}_8Br^{a}_6]^{2-}$ units. See Scheme 1 for atom labeling. Relative energies (in eV and cm^{-1}) are given compare to the ground state S_0 energy.

$[Mo_6Br^{i}_8Br^{a}_6]^{2-}$	S_0	T_1	T_2	T_3	T_4
Symmetry	O_h	C_1	C_s	C_s	C_{2v}
Distances					
Mo-Mo	2.655				
Mo1-Mo2		2.631	2.630	2.627	**3.082**
Mo1-Mo4		2.670	2.667	2.669	2.664
Mo1-Mo5		**2.752**	**2.745**	**2.756**	**2.713**
Mo1-Mo6		2.654	2.651	2.653	**2.713**
Mo2-Mo3		2.670	2.667	2.669	2.664
Mo2-Mo5		**2.750**	**2.745**	**2.756**	**2.713**
Mo2-Mo6		2.655	2.651	2.653	**2.713**
Mo3-Mo4		2.632	2.630	2.634	2.684
Mo3-Mo5		**2.744**	**2.745**	**2.732**	2.636
Mo3-Mo6		2.655	2.651	2.652	2.636
Mo4-Mo5		**2.744**	**2.745**	**2.732**	2.664
Mo4-Mo6		2.654	2.651	2.652	2.636
average	*2.655*	*2.684*	*2.682*	*2.672*	*2.710*
Mo-Br^{i}	2.642				
125 face		2.666 2.667 **2.921**	2.664 2.664 **2.913**	2.662 2.662 **2.920**	2.686 2.686 2.642
235 face		2.675 2.677 2.634	2.674 2.674 2.631	2.667 2.677 2.637	2.602 2.664 2.683
345 face		2.667 2.667 **2.910**	2.664 2.664 **2.913**	2.663 2.663 **2.890**	2.642 2.642 2.653
145 face		2.674 2.678 2.634	2.674 2.674 2.631	2.667 2.677 2.637	2.602 2.664 2.683
126 face		2.646 2.645 2.640	2.643 2.643 2.637	2.643 2.643 2.636	2.686 2.686 2.642
236 face		2.647 2.646 2.641	2.644 2.644 2.638	2.643 2.645 2.639	2.602 2.664 2.683
346 face		2.645 2.646 2.640	2.643 2.643 2.637	2.644 2.644 2.636	2.642 2.642 2.653
146 face		2.647 2.647 2.641	2.644 2.644 2.638	2.643 2.645 2.639	2.602 2.664 2.683
average	*2.642*	*2.675*	*2.672*	*2.672*	*2.654*
Mo-Br^{a}	2.653				
Mo_1-Br^{a}		2.653	2.648	2.645	2.630
Mo_2-Br^{a}		2.653	2.648	2.645	2.630
Mo_3-Br^{a}		2.653	2.648	2.645	2.659
Mo_4-Br^{a}		2.653	2.648	2.645	2.659
Mo_5-Br^{a}		**2.614**	**2.608**	**2.605**	2.647
Mo_6-Br^{a}		2.663	2.658	2.654	2.647
average	*2.653*	*2.648*	*2.643*	*2.646*	*2.654*
$E_{relative}$ (eV)	0.000	1.909	1.921	1.934	2.007
$E_{relative}$ (cm^{-1})	0	15400	15490	15600	16190

Triplet excited states. As stated above, the difference in energy between the FC-triplet excited states and the ground state are much higher than the experimental emission energies. Additionally, the experimental shift between absorption and emission is really large revealing important changes during the de-excitation processes. Among all the possible changes, geometrical relaxations (atomic motions) have to be considered at first. We thus performed geometry relaxations of the first excited triplet states by two different methods. On one hand, the triplet excited-state structures have been optimized using analytic TD-DFT gradients (12 firsts). On the other hand, 10 different starting geometries were built on the basis of the bonding / anti-bonding character of the orbitals involved to describe the first FC-triplet excited states. The geometry optimizations led to only four different geometries for which the local minimum character was proven by vibrational frequency calculations. Their main geometrical and energy characteristics are given in Table 3 and described in Scheme 1. At that stage, it has to be emphasized that we cannot rule out the existence of other stable triplet states with different geometrical arrangements in the same region of energy. To obtain exhaustive results, a full exploration of the potential energy surface of the triplet states would be necessary.

These calculations show asymmetrical distortions from O_h symmetry of the triplet geometries. A symmetry-based triplet geometry searches would have failed in finding these geometries. Unfortunately, it is impossible to handle full energy surface characterizations considering the number of geometrical parameters to consider in absence of symmetry. For all triplet geometries ($T_{1\text{-}4}$), elongations of the metal-metal bonds are observed in full agreement with the anti-bonding nature of the populated LUMOs (see Scheme 1). The geometries of the relaxed T_1, T_2 and T_3 show a lengthening of Mo-Mo distances corresponding to an outstretching of one vertex away from the basal square plane. In the case of T_2, this elongation is co-axial to the C_4 axis and is accompanied by the shortening of two opposite Mo-Mo bonds of the basal plane (see Scheme 1). The Mo-Br bonds are consequently modified with an average lengthening of the inner bonds and a shortening of the apical ones. For example, for T_2, the apical Mo-Br bond of the outstretched Mo atom (Mo5) is of 2.608 Å (2.653 Å for S_0). T_1 is the most stable arrangement (C_1). The main geometrical changes of T_1 compare to T_2 is of 0.008 Å (Mo5-Br^i) and it corresponds to a deviation of the distortion from the C_4 axis. T_3 shows the same type of deviation from T_2 but keeping a symmetry plane. Even though the geometries of T_1, T_2 and T_3 are quite similar, the differences in energy between them allow considering them as distinct states at our level of theory. Vibrational frequencies are also different (see below).

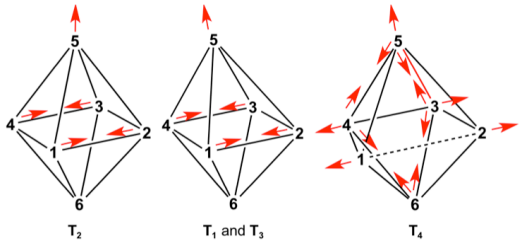

Scheme 1. Metal-metal distortions encountered in the geometry relaxation of the first triplet spin states.

It is worth noting that the groups of T. G. Gray and D. G. Nocera mentioned triplet distortion from O_h to D_{4h} or to D_{2h} for the rhenium-chalcogen and tungsten-halide analogs.[18,33] The calculated emission energies they obtained are higher than the experimental ones. They also mentioned that multi-state luminescence can explain theory/experiment discrepancies. Comparing with our results, we can deduce that less symmetric triplet states exist also in rhenium and tungsten series.

The spin-density plots of $T_{1\text{-}4}$ are given in Fig. S7, and the Mo Mulliken atomic spin-densities in Table S5. The spin density of the Mo atom which is outstretched from square basal plane (Mo_5, see Scheme 1) is of ~1.7 e for T_1, T_2 and T_3, the rest of the spin-density being delocalized. The partial breaking of one Mo-Mo bond (Mo1-Mo2 = 3.082 vs 2.655 Å in S_0) in T_4 (not observed in $T_{1\text{-}3}$) leads to a different spin-density localization with almost one unpaired electron on Mo1 and Mo2.

The gain in energy obtained after these geometrical relaxations is larger than 0.38 eV (3090 cm^{-1}). It has to be emphasized that emission occurs from these geometries. Emission energies cannot thus be calculated just by subtracting the energies of the triplet to the one of the ground state. The emission energies associated with those relaxed triplet states can be evaluated by Tamm-Dancoff SO coupling DFT calculations (see computational details). It has to be stressed that the calculated SO splits of the triplet states are negligible (less than 0.001 eV) and cannot explain the multiple-component spectra as postulated by Azumi and coworkers.[17] Our calculations allow also to evaluate the lifetime of the spontaneous emission (see Table 4). These are of the order of 240 to 450 µs for the most probable emissions. Interestingly, the emission energy does not follow the same order as the relative energy of the triplet state from which it is issued (see Table 4). The emission energy calculated for T_4 is of 11360 cm^{-1} (1.408 eV); a value close to the experimental emission component λ_2 (11700 cm^{-1}). The emission energies calculated from T_1, T_2 and T_3 are respectively of 13710, 13850 and 13900 cm^{-1} (1.700, 1.717, 1.724 eV); these values are close to the experimental component λ_1 (13850 cm^{-1}, TRPL 12 K). At that stage, it is difficult to discriminate between them taking into account the accuracy of the calculations and the fact that the solid-state matrix certainly influences the geometrical relaxation of the triplet. Moreover, one cannot exclude that λ_1 is due to several close-lying emissions. The calculated spontaneous radiation lifetimes which do not take into account the non-radiative de-excitation processes are really similar and do not help to discriminate between systems.

Table 4. Relative energies E_{rel} (eV) SO corrected compare to the ground state of the lowest optimized state of $[Mo_6Br^i_8Br^a_6]^{2-}$ (SO split triplet). First emission E_{em} (eV and cm^{-1}) energies, associated oscillator strength (f) and spontaneous radiation lifetime (µs).

State	E_{rel} (eV)	E_{em} (eV)	E_{em} (cm^{-1})	f	Lifetime (µs)
T_1	1.909	1.700	13710	$6.37\ 10^{-6}$	1260
		1.700		$2.39\ 10^{-5}$	334
		1.702		$1.89\ 10^{-5}$	422
T_2	1.921	1.717	13850	$1.88\ 10^{-6}$	4150
		1.717		$3.30\ 10^{-5}$	237
		1.717		$2.21\ 10^{-5}$	353
T_3	1.934	1.724	13900	$6.80\ 10^{-6}$	1140
		1.724		$2.77\ 10^{-5}$	279
		1.724		$2.18\ 10^{-5}$	355
T_4	2.007	1.407	11360	$2.38\ 10^{-12}$	-
		1.408		$1.38\ 10^{-5}$	845
		1.408		$2.61\ 10^{-5}$	446

It has to be emphasized that the spectroscopic features of the triplet states are different from the ground state and also from each other. The simulation of the absorption spectra of the triplet excited states are given in Supporting Information. They show that contrarily to singlet ground state, the triplet excited states absorb between 15400 and 20000 cm^{-1} (500 to 650 nm). Their simulated spectra, sketched in Fig. S6, are quite similar which makes triplet absorption not a good spectroscopy to differentiate them. Vibrational-based spectroscopy is more sensitive to small geometrical changes. The simulated IR spectra calculated for S_0, T_1, T_2 and T_4 are shown in Fig. 8. Clearly, time-resolved fast-Fourier transformed IR or Raman spectroscopies should be appropriate tools to reveal the nature

of the triplet states involved in the de-excitation process by direct comparison to the calculated ones.

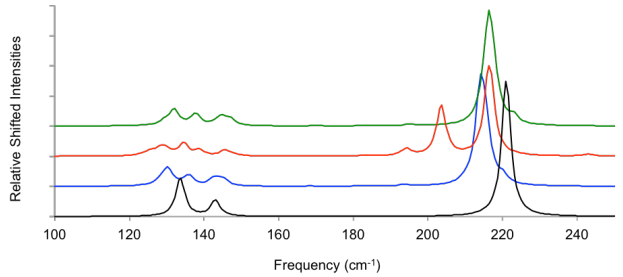

Fig. 8. Simulated IR spectra of S_0 in black, of T_1 (blue), T_2 (red) and T_4 (green) obtained from DFT calculations. T_3 shows an IR simulated spectra similar to T_2.

Unusual temperature dependent photo-physical properties were recently explained by thermal population of excited states in inorganic systems.[34] To evaluate such thermal processes, we looked for the transition states that connect T_4 to $T_{1\text{-}3}$. This allows calculating the potential energy barrier of thermal interconversion between triplet states. One common transition state was found. Searches were performed by intrinsic reaction path and transition state calculations. The Cartesian coordinates of this common transition state are given in Supporting Information (Table S6). The associated energy barrier is of 0.035 eV and corresponds to a Boltzmann population ratio of 0.25 at RT and no population of $T_{1\text{-}3}$ at 12 K.

Discussion

The combination of the experimental and quantum chemical results reported here allow to draw a clearer picture of the non-radiative de-excitation mechanisms occurring after excitation of the $[Mo_6Br^i_8Br^a_6]^{2-}$ cluster unit. Both the PL excitation mapping and the time resolved PL show that the emission is composed of at least two discrete components. Vibronic coupling could be argued to explain this but the red shift observed between the spectra recorded at room temperature and at 12 K invalidates this hypothesis. Moreover, all IR vibrational frequencies are lower than 400 cm^{-1} for those solids, and thus cannot account for the two-component emission band (minimum difference between maxima = 830 cm^{-1}).[19] Impurities or energy-trapping in the solids could also be argued but the two-component nature of the emission is found both in solid-state (in two different structures) and in solution (see Fig. 2, S2 and Table S1). This unambiguously proves that the emission properties originate from the cluster unit.

From the Steady State PL and TRPL, it appears that several emission processes occur almost simultaneously. Part or all of those processes (depending on the quantum yield) lead to relaxed triplet states that are emissive. The spectral feature is thus composed of several components. Their relative contribution is temperature-dependent illustrating the existence of several competitive non-radiative de-excitation paths. This does not follow the usual empirical Kasha's rules which states that the non-radiative de-excitations always end up to the lowest excited state. This postulate implies that only one-component emission are possible. It is not the case for $[Mo_6Br^i_8Br^a_6]^{2-}$-containing systems for which our experimental PL measurements show clearly two components. Evidences of two emitting states were reported for rhenium analogs by T. G. Gray *et al.* for $[Re_6S^i_8]^{2+}$ and $[Re_6Se^i_8]^{2+}$ clusters.[33c] The latter findings associated with the fact that luminescence occurs after several picoseconds evidence that atomic relaxations occur, as suggested by these authors.

SO TD-DFT calculations, associated with geometry optimization of excited states are now available in commercial quantum chemical programs, allowing accessing to more quantitative emission energies. We used this methodology to calculate the optimized geometry of the lowest triplet excited states. Important deformations of the octahedral Mo_6 cage are observed, either by an outstretching of an apex away from the square plane of the octahedron (C_{2v}, C_s, C_1) or by an elongation of one Mo-Mo bond (C_s symmetry). An important amount of energy is gained upon those different relaxations (~0.3-0.4 eV). The emission energies calculated from the 4 lowest triplet states we found are in the range of the experimental data. At this stage, we cannot rule in favor of one of the three first triplet states to describe the first experimental component **1** (several triplet states could be involved since they are close in energy and geometry). For the second component **2**, the calculated emission of T_4, which geometry corresponds to the elongation of one Mo-Mo, is in good agreement with the experimental measurements (11360 cm^{-1} vs 11700 cm^{-1}).

The large energy difference between absorption and emission observed experimentally is thus a consequence of the important stabilizations of the emissive triplet excited states upon geometrical relaxation as illustrated in Scheme 2. Emission occurs indeed from those geometrical arrangements. This implies also that the emission from a triplet state T_y (see Scheme 2) can be lower in energy than the one of the lower lying triplet state T_1 since *i*) the geometrical relaxation can be more important in T_y than in T_1 and *ii*) the singlet-state energy to consider is the one at the relaxed triplet geometry. Considering the recent literature in the domain,[34] a thermal population of the triplet excited states has to considered since their lifetime is long enough (see Scheme 2).

The DFT study reveals that the calculated energy barrier connecting T_4 (the highest triplet excited state which emits lower energy; associated to the experimental component **2**) to $T_{1\text{-}3}$ (**1**) is too high to allow a thermal population at low temperature (no thermal equilibrium below 60 K). Nevertheless, the experimental TRPL emission spectra shown in Fig. 5 and 6 show unambiguously that at 12 K both emissions are present (roughly one third issued from λ_2). On the basis of these experimental evidences and DFT calculations, we can conclude that several non-radiative de-excitations occur at low temperature leading to dual (or multiple) emission. At RT, thermal equilibrium most probably occurs (calculated Boltzmann population ratio of 0.25). Nevertheless, the optical de-excitation processes are also affected by temperature (population of vibrational states and thus additional internal conversion possibilities) preventing us from giving any additional findings. Nevertheless, the differences observed

experimentally between steady-state PL and TRPL clearly illustrate a complex phenomenon in which additionally to thermal processes, absorption of the excited states would have to be considered (steady-state PL are done at continuous irradiation).

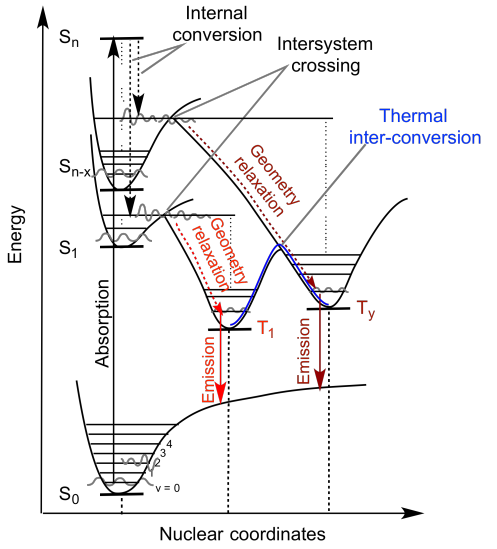

Scheme 2. Schematic Jablonski-type diagram of de-excitation via two paths leading to the emission from T_1 and any emissive T of higher energy labeled T_y with a possible thermal inter-conversion.

At this stage, it has to be emphasized that the environment of the cluster unit has an influence on the relaxation process. Indeed, the counter-cation arrangements and the crystal-packing certainly influence *i*) the non-radiative de-excitation for which the vibrations are involved and *ii*) the geometrical relaxation of the triplet state. Kinetic and dynamic relaxations are crystal dependent. The same reason probably explains the differences in the phosphorescence lifetime values between the two solids.

Conclusions

Our multi-approach study reveals that vibronic coupling and spin-orbit effects cannot explain the experimental PL measurements obtained for two $[Mo_6Br^i_8Br^a_6]^{2-}$-based solids. Our experiments show unambiguously that at least two-excited states are responsible for the emission of $(TBA)_2[Mo_6Br^i_8Br^a_6]$ and $(Cs)_2[Mo_6Br^i_8Br^a_6]$ in solution and in solid-state. By a combined experimental and quantum chemical study, we show that important geometrical relaxations of the $[Mo_6Br^i_8Br^a_6]^{2-}$ excited unit occur before emission. Therefore, one can conclude that the discrepancies previously found between published theoretical studies and experimental values are not due to a breakdown of DFT and TD-DFT but rather to the limitation imposed by the chosen models (no relaxation or high symmetry constraints for the triplet state geometry). Indeed, our quantum chemical study led to calculated emission energy values that are in good agreement with the experimental measurements when considering low-symmetry geometrical relaxations.

The calculated electronic excitations and vibrational frequencies performed on the triplet excited states reveal that it will be possible to identify the nature and the number of the excited states involved in the de-excitation process (before and during emission) by ultrafast time-resolved IR or Raman spectroscopies. Finally, our work allows postulating that, by modifying the local environment of the cluster (geometrical constraints, electrostatic external field) or changing the excitation procedure (time of irradiation, irradiation wavelength, temperature), one can access to different excited states. This tunability is an important feature that explains the numerous examples of applications for materials containing octahedral metallic clusters. This contribution to the comprehension of the de-excitation/emission processes of $[Mo_6Br^i_8Br^a_6]^{2-}$ containing systems provides new tools to design target (hybrid) materials notably by constraining the relaxation of the excited states.

Acknowledgements

Frédéric Geschier is warmly acknowledged for technical assistance. A.G. is grateful for support from the Region Pays de la Loire (NanoFonc network). We acknowledge the C'Nano Nord-Ouest network for support of this work. Computations were performed using GENCI HPC resources (2014-15-80649).

Notes and references

1 (a) S. Cordier, F. Dorson, F. Grasset, Y. Molard, B. Fabre, H. Haneda, T. Sasaki, M. Mortier, S. Ababou-Girard, C. Perrin, *J. Clust. Sci.*, 2009, **20**, 9; (b) S. Cordier, Y. Molard, K. Brylev, Y. Mironov, F. Grasset, B. Fabre, N. G. Naumov, *J. Cluster Sci.*, 2015 **81**, 26; (c) S. Cordier, F. Grasset, Y. Molard, M. Amela-Cortes, R. Boukherroub, S. Ravaine, M. Mortier, N. Ohashi, N. Saito, H. Haneda, *J. Inorg. Organomet. Polym. Mater.*, 2015, **25**, 189.

2 (a) T. Caillat, J.-P. Fleurial, G. Snyder, *Solid State Sci.*, 1999, **1**, 535; (b) T. Zhou, B. Lenoir, M. Colin, A. Dauscher, R. Al Rahal Al Orabi, P. Gougeon, M. Potel, E. Guilmeau, *App. Phys. Lett.*, 2011, **98**, 162106; (c) P. Gougeon, P. Gall, R. Al Rahal Al Orabi, B. Fontaine, R. Gautier, M. Potel, T. Zhou, B. Lenoir, M. Colin, C. Candolfi, A. Dauscher, *Chem. Mater.*, 2012, **24**, 2899; (d) T. Zhou, M. Colin, C. Candolfi, C. Boulanger, A. Dauscher, E. Santava, J. Hejtmanek, P. Baranek, R. Al Rahal Al Orabi, M. Potel, B. Fontaine, P. Gougeon, R. Gautier, B. Lenoir, *Chem. Mater.*, 2014, **26**, 4765; (e) R. Al Rahal Al Orabi, P. Gougeon, P. Gall, B. Fontaine, R. Gautier, M. Colin, C. Candolfi, A. Dauscher, J. Hejtmanek, B. Malaman, B. Lenoir, *Inorg. Chem.*, 2014, **53**, 11699.

3 (a) S. Boursicot, V. Bouquet, I. Péron, T. Guizouarn, M. Potel, M.Guilloux-Viry, *Solid State Sci.*, 2012, **14**, 719; (b) V. Bouquet, M. Guilloux-Viry, M. Potel, C. Boulanger, J.-M. Lecuire, A. Bombard, US Patent n° 61/654,485.

4 (a) A. W. Maverick, J. S. Najdzionek, D. Mackenzie, D. G. Nocera, H. B. Gray, *J. Am. Chem. Soc.*, 1983, **105**, 1878; (b) M. K. Simsek, D. Bublitz, W. Preetz, *Z. Anorg. Allg. Chem.*, 1997, **623**, 1885; (c) L. G. Beauvais, M. P. Shores, J. R. Long, *Chem. Mater.*, 1998, **10**, 3783; (d) G. Pilet, S. Cordier, S. Golhen, C. Perrin, L. Ouahab, A. Perrin, *Solid State Sci.*, 2003, **5**, 1263–1270; (e) S. S. Yarovoi, Y. V. Mironov, D. Y. Naumov, Y. V. Gatilov, S. G. Kozlova, S.-J. Kim, V. E. Fedorov, *Eur. J. Inorg. Chem.*, 2005, 3945; (f) K. Kirakci, P. Kubat, J. Langmaier, T. Polivka, M. Fuciman, K. Fejfarova, K. Lang, *Dalton Trans.*, 2013, **42**, 7224–7232; (g) A.

Gandubert, K. A. Brylev, T. T. Nguyen, N. G. Naumov, N. Kitamura, Y. Molard, R. Gautier, S. Cordier, *Z. Anorg. Allg. Chem.*, 2013, **639**, 1756; (h) M. Amela-Cortes, S. Cordier, N. G. Naumov, C. Meriadec, F. Artzner, Y. Molard, *J. Mater. Chem. C*, 2014, **2**, 9813.

5 (a) F. Grasset, F. Dorson, S. Cordier, Y. Molard, C. Perrin, A.-M. Marie, T. Sasaki, H. Haneda, Y. Bando, M. Mortier, *Adv. Mater.*, 2008, **20**, 143; (b) T. Aubert, A. Burel, M.-A. Esnault, S. Cordier, F. Grasset, F. Cabello-Hurtado, *J. Hazard. Mater.*, 2012, **219**, 111; (c) T. Aubert, F. Cabello-Hurtado, M.-A. Esnault, C. Neaime, D. Lebret-Chauvel, S. Jeanne, P. Pellen, C. Roiland, L. Le Pollès, N. Saito, K. Kimoto, H. Haneda, N. Ohashi, F. Grasset, S. Cordier, *J. Phys. Chem. C*, 2013, **117**, 20154; (d) N. Nerambourg, T. Aubert, C. Neaime, S. Cordier, M. Mortier, G. Patriarche, F. Grasset, *J. Colloid Int. Sci.*, 2014, **424**, 132.

6 (a) Y. Molard, F. Dorson, V. Circu, T. Roisnel, F. Artzner, S. Cordier, *Angew. Chem. Int. Ed.*, 2010, **49**, 3351; (b) A. S. Mocanu, M. Amela-Cortes, Y. Molard, V. Circu, S. Cordier, *Chem. Comm.*, 2011, **47**, 2056; (c) Y. Molard, A. Ledneva, M. Amela-Cortes, V. Circu, N. G. Naumov, C. Meriadec, F. Artzner, S. Cordier, *Chem. Mater.*, 2011, **23**, 5122; (d) M. A. Cortes, F. Dorson, M. Prevot, A. Ghoufi, B. Fontaine, F. Goujon, R. Gautier, V. Circu, C. Meriadec, F. Artzner, H. Folliot, S. Cordier, Y. Molard, *Chem. Eur. J.*, 2014, **20**, 8561; (e) S. K. Nayak, M. Amela-Cortes, C. Roiland, S. Cordier, Y. Molard, *Chem. Commun.*, 2015, **51**, 3774. (f) M. Prévot, M. Amela-Cortes, S. K. Manna, S. Cordier, T. Roisnel, H. Folliot, L. Dupont, Y. Molard *J. Mater. Chem C*, **2015**, *3*, 5111.

7 Y. Zhao, R. R. Lunt, *Adv. Energy Mater.*, 2013, **3**, 1143–1148.

8 Y. Molard, C. Labbe, J. Cardin, S. Cordier, *Adv. Funct. Mater.*, 2013, **23**, 4821.

9 (a) F. Grasset, Y. Molard, S. Cordier, F. Dorson, M. Mortier, C. Perrin, M. Guilloux-Viry, T. Sasaki, H. Haneda, *Adv. Mater.*, 2008, **20**, 1710; (b) T. Aubert, N. Nerambourg, N. Saito, H. Haneda, N. Ohashi, M. Mortier, S. Cordier, F. Grasset, *Part. Part. Syst. Charact.*, 2013, **30**, 90.

10 (a) A. Garreau, F. Massuyeau, S. Cordier, Y. Molard, E. Gautron, P. Bertoncini, E. Faulques, J. Wery, B. Humbert, A. Bulou, J.-L. Duvail, *ACS Nano*, 2013, **7**, 2977; (b) M. Amela-Cortes, A. Garreau, S. Cordier, E. Faulques, J.-L. Duvail, Y. Molard, *J. Mater. Chem. C*, 2014, **2**, 1545.

11 (a) A. Barras, S. Cordier, R. Boukherroub, *Appl. Cat. B-Env.*, 2012, **123**, 1; (b) S. Kumar, O. P. Khatri, S. Cordier, R. Boukherroub, S. L. Jain, *Chem. - Eur. J.*, 2015, **21**, 3488; (c) A. Barras, M. R. Das, R. R. Devarapalli, M. V. Shelke, S. Cordier, S. Szunerits, R. Boukherroub, *Appl. Catal. B-Environ.*, 2013, **130**, 270; (d) P. Kumar, S. Kumar, S. Cordier, S. Paofai, R. Boukherroub, S. L. Jain, *RSC Adv.*, 2014, **4**, 10420.

12 (a) S. Cordier, C. Perrin, M. Sergent, *Z. Anorg. Allg. Chem.*, 1993, **619**, 621; (b) K. Kirakci, S. Cordier, C. Perrin, *Z. Anorg. Allg. Chem.*, 2005, **631**, 411.

13 A. W. Maverick, H. B. Gray, *J. Am. Chem. Soc.*, 1981, **103**, 1298.

14 M. N. Sokolov, M. A. Mihailov, E. V. Peresypkina, K. A. Brylev, N. Kitamura, V. P. Fedin, *Dalton Trans.*, 2011, **40**, 6375.

15 Y. Saito, H. K. Tanaka, Y. Sasaki, T. Azumi, *J. Phys. Chem.*, 1985, **89**, 4413.

16 L. M. Robinson, R. L. Bain, D. F. Shriver, D. E. Ellis, *Inorg. Chem.*, 1995, **34**, 5588.

17 R. Ramirez-Tagle, R. Arratia-Pérez, *Chem. Phys. Lett.*, 2008, **460**, 438.

18 T. G. Gray, *Chem. Eur. J.*, 2009, **15**, 2581.

19 D. Bublitz, W. Preetz, *Z anorg. Allg. Chem.*, 1996, **622**, 1107.

20 A. Garreau, K. Costuas, S. Cordier, E. Faulques, J.-L. Duvail, A. Bulou, to be published.

21 (a) G. te Velde, F. M. Bickelhaupt, E. J. Baerends, C. Fonseca Guerra, S. J. A. van Gisbergen, J. G. Snijders, T. Ziegler, *J. Comput. Chem.*, 2001, **22**, 931; (b) C. Fonseca Guerra, J. G. Snijders, G. te Velde, E. J. Baerends, *Theor. Chem. Acc.*, 1998, **99**, 391; (c) Amsterdam Density Functional (ADF) program, release 2014.01. SCM, Theoretical Chemistry, Vrije Universiteit, Amsterdam, The Netherlands, http://www.scm.com/.

22 Y. Zhang, W. Yang, *Phys. Rev. Lett.*, 1998, **80**, 890.

23 S. H. Vosko, L. Wilk, M. Nusair, *Can. J. Phys.*, 1980, **58**, 1200.

24 (a) E. van Lenthe, A. E. Ehlers, E. J. Baerends, *J. Chem. Phys.*, 1999, **110**, 8943; (b) E. van Lenthe, E.; E. J. Baerends, *J. Comput. Chem.*, 2003, **24**, 1142.

25 S. Hirata, M. Head-Gordon, *Chem. Phys. Lett.*, 1999, **314**, 291.

26 (a) E. van Lenthe, A. E. Ehlers, E. J. Baerends, J. G. Snijders, *J. Chem. Phys.*, 1993, **99**, 4597; (b) E. van Lenthe, A. E. Ehlers, E. J. Baerends, J. G. Snijders, *J. Chem. Phys.*, 1994, **101**, 9783; (c) E. van Lenthe, A. E. Ehlers, E. J. Baerends, J. G. Snijders, *J. Chem. Phys.*, 1996, **105**, 6505; (d) E. van Lenthe, R. van Leeuwen, E. J. Baerends, J. G. Snijders, *Int. J. Quantum Chem.*, 1996, **57**, 281.

27 (a) S. J. Clark, M. D. Segall, C. J. Pickard, P. J. Hasnip, M. I. J. Probert, K. Refson, M.C. Payne, *Z. Kristallogr.*, 2005, **220**, 567; (b) M. D. Segall, P. J. D. Lindan, M. J. Probert, C. J. Pickard, P. J. Hasnip, S. J. Clark, M. C. Payne, *J. Phys. Condens. Matter*, 2002, **14**, 2717.

28 J. P. Perdew, K. Burke, M. Ernzerhof, *Phys. Rev. Lett.*, 1996, **77**, 3865.

29 A. Tkatchenko, M. Scheffler, *Phys. Rev. Lett.*, 2009, **102**, 073005.

30 (a) D. D. Koelling, B. N. Harmon, *J. Phys. C*, 1977, **10**, 3107; (b) S. Louie, S. Froyen, M. Cohen, *Phys. Rev. B*, 1982, **26**, 1738.

31 R. Gautier, J.-F. Halet, J.-Y. Saillard, Computational Methods: Transition Metal Clusters, in "Encyclopedia of Inorganic Chemistry", eds. E. I Solomon, R. B. King, R. A. Scott, Wiley, Chichester, 2009, p. 433-452.

32 (a) T. Hughbanks, R. Hoffmann, *J. Am. Chem. Soc.*, 1983, **105**, 1150; (b) T. Hughbanks, *Prog. Solid State Chem.*, 1989, **19**, 329; (c) R. Gautier, E. Furet, J.-F. Halet, Z. Lin, J.-Y. Saillard, Z. Xu, *Inorg. Chem.*, 2002, **41**, 796; (d) P.-D. Fan, P. Deglmann, R. Ahlrichs, *Chem. Eur. J.*, 2002, **8**, 1059.

33 (a) T. G. Gray, C. M. Rudzinski, D. G. Nocera, R. H. Holm, *Inorg. Chem.*, 1999, **38**, 5932; (b) T. G. Gray, C. M. Rudzinski, E. E. Meyer, R. H. Holm, D. G. Nocera, *J. Am. Chem. Soc.*, 2003, **125**, 4755; (c) T. G. Gray, C. M. Rudzinski, E. E. Meyer, D. G. Nocera, *J. Phys. Chem. A*, 2004, **108**, 3238.

34 (a) Y.-S. Yeh, Y.-M. Cheng, P.-T. Chou, G.-H. Lee, C.-H. Yang, Y. Chi, C.-F. Shu, C.-H. Wang, *ChemPhysChem*, 2006, **7**, 2294; (b) A. Steffen, K. Costuas, A. Boucekkine, M.-H. Thibault, A. Beeby, A. S. Batsanov, A. Charaf-Eddin, D. Jacquemin, J.-F. Halet, T. B. Marder, *Inorg. Chem*, 2014, **53**, 7055. (c) D. Escudero, W. Thiel, *Inorg. Chem*., 2014, **53**, 11015; (d) D. Escudero, D. Jacquemin, *Dalton Trans.*, 2015, **44**, 8346 and references therein; (e) Q. Benito, X. F. Le Goff, G. Nocton, A. Fargues, A. Garcia, A. Berhault, S. Kahlal, J.-Y. Saillard, C. Martineau, J. Trébosc, T. Gacoin, J.-P Boilot, S. Perruchas, *Inorg. Chem.*, 2015, **54**, 4483.